Research Article | Vol. 28, No. 21 / 12 October 2020 / Optics Express 30889

Optics EXPRESS

Plasmonic nanoarcs: a versatile platform with tunable localized surface plasmon resonances in octave intervals

KUNYI ZHANG,[1] ANDREW P. LAWSON,[1] CHASE T. ELLIS,[2] MATTHEW S. DAVIS,[3] THOMAS E. MURPHY,[3,4] HANS A. BECHTEL,[5] JOSEPH G. TISCHLER,[2] AND ODED RABIN[1,4,*]

[1] Department of Materials Science and Engineering, University of Maryland, College Park, Maryland 20742, USA
[2] U.S. Naval Research Laboratory, Washington, DC 20375, USA
[3] Department of Electrical and Computer Engineering, University of Maryland, College Park, Maryland 20742, USA
[4] Institute for Research in Electronics and Applied Physics, University of Maryland, College Park, Maryland 20742, USA
[5] Advanced Light Source Division, Lawrence Berkeley National Laboratory, Berkeley, California 94720, USA
[*] oded@umd.edu

Abstract: The tunability of the longitudinal localized surface plasmon resonances (LSPRs) of metallic nanoarcs is demonstrated with key relationships identified between geometric parameters of the arcs and their resonances in the infrared. The wavelength of the LSPRs is tuned by the mid-arc length of the nanoarc. The ratio between the attenuation of the fundamental and second order LSPRs is governed by the nanoarc central angle. Beneficial for plasmonic enhancement of harmonic generation, these two resonances can be tuned independently to obtain octave intervals through the design of a non-uniform arc-width profile. Because the character of the fundamental LSPR mode in nanoarcs combines an electric and a magnetic dipole, plasmonic nanoarcs with tunable resonances can serve as versatile building blocks for chiroptical and nonlinear optical devices.

1. Introduction

Plasmonic nanoantennas possess fascinating optical properties with a wide range of applications in molecular spectroscopy [1–3] and photonics technologies [4,5]. The novel optical properties arise from the interaction between light and surface plasmons. Localized surface plasmon resonances (LSPRs) of plasmonic nanoantennas can be excited by light with proper frequency and polarization, resulting in a strongly-enhanced local electromagnetic field. The frequencies of these resonances depend strongly on the plasmonic object shape, size, and material as well as the dielectric environment [2,3]. Plasmonic effects have been investigated with various metallic nanostructures, including centrosymmetric nanorods [6–8] and nanodisks [9], and non-centrosymmetric nanocrescents [10,11], split-ring resonators [12–16], V-shaped, L-shaped and U-shaped antennae [17–19], and multimers [20–22]. Methods for predicting the frequencies of LSPRs of plasmonic nanoantennas and design rules for tuning these frequencies are of general interest. However, the attribution of LSPR frequencies to non-centrosymmetric nanoantennas is often carried out on a case-by-case basis via numerical simulations or trial-and-error experimentation.

Plasmonic nanorods (Fig. 1(a)) are uniaxial nanostructures that act as microscopic antennae inasmuch as they absorb, scatter and emit electromagnetic radiation of a particular polarization at characteristic frequencies that correspond to the dipolar LSPR modes. The ease of nanorod

#403728 https://doi.org/10.1364/OE.403728
Journal © 2020 Received 6 Aug 2020; revised 10 Sep 2020; accepted 13 Sep 2020; published 1 Oct 2020

Optics EXPRESS

fabrication, via chemical synthesis [7,23–25] or lithography [26–30], and the ability to modify their optical properties by adjusting their aspect ratios [26,31,32] have motivated numerous studies that focus on nanorods and their use as building blocks for more complex plasmonic structures and metamaterials [6,33–36]. Polarization-dependent spectroscopy studies of nanorods have identified longitudinal and transverse LSPR modes with oscillating electric dipoles oriented along the long and short axis of the nanorod, respectively. The longitudinal LSPRs in plasmonic nanorods are highly tunable (across the visible and infrared spectra, for Au and Ag nanorods) by adjusting the nanorod length, while the transverse LSPRs typically resonate at significantly higher frequencies and their tunability is negligible for high aspect ratio nanostructures [32,37]. Due to symmetry, the even-order LSPR modes in nanorods are dark modes.

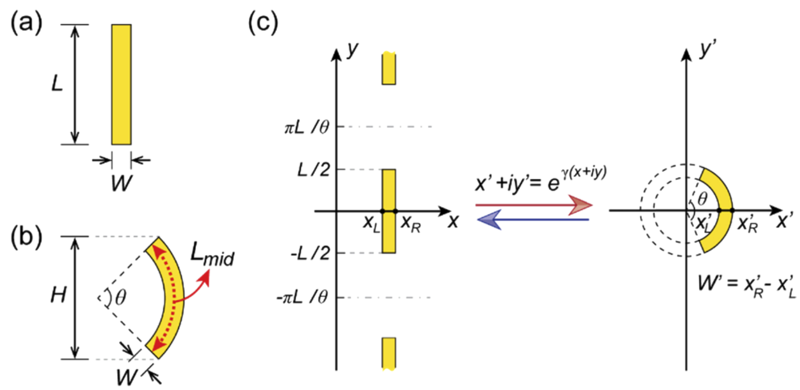

Fig. 1. Schematic of (a) the nanorod geometry and (b) the nanoarc geometry, with definitions for the rod length L, the rod/arc width W, the arc height H, central angle θ, and mid-arc length L_{mid}. (c) The 2D conformal transformation that maps a periodic array of rods to an arc, and vice versa. The coordinates in the transformed plane are primed to distinguish them from those in the original plane.

Plasmonic nanoarcs (Fig. 1(b)), curved metal strips on dielectric substrates, have a number of attributes that distinguish them from (straight) nanorods. Due to the lower symmetry of nanoarcs (C_{2v} point group), their optical attenuation spectra exhibit twice the number of longitudinal LSPR signatures compared to nanorods (D_{2h} point group). In nanoarcs the odd- and even-order LSPR modes correspond to orthogonal polarization states resulting in coupling to radiation with polarization in all in-plane directions, with potential implications for filtering and polarization conversion effects [38,39]. The near-field and far-field scattering pattern of nanoarcs can be directional – an exciting feature for plasmonics circuitry [40,41]. Nanoarcs can be considered as an intermediate geometry linking straight nanorod antennae and nanoscale split-ring resonators (SRR) through the process of bending [42]. A series of nanoarcs with varying central angles is ideal for the study of the emergence of the magnetic character of the surface plasmon mode, which is a strong and useful feature in SRRs [43–45]. Last, the simultaneous presence of oscillating electric and magnetic dipoles upon excitation of the fundamental longitudinal LSPR mode makes the nanoarc an ideal building block for chiroptical and nonlinear optical metamaterials [46,47].

Here, we report a study of LSPRs in plasmonic nanoarcs employing transformation optics (TO) design, Fourier-transform infrared (FTIR) spectroscopy measurements, and numerical simulations. The nanoarcs investigated are sectors of circular rings with rectangular cross-section. As such, their geometry is fully described by 4 parameters, i.e., height H, width W, thickness t and central angle θ (Fig. 1(b)). This family of structures was chosen because their fabrication is feasible by means of standard electron-beam lithography (EBL) and metal film lift-off processes, their shape parameters can be tuned systematically, and straightforward comparisons with rectangular

Optics EXPRESS

cross-section nanorods can be made. Related structures, namely V-shaped nanoantennas [48–50] and nanocrescents [51,52], have been previously made by direct lithography and template shadow evaporation, respectively. In contrast to the nanoarcs reported here, each of those nanostructures has 2 sharp corners that under proper illumination conditions are associated with the sub-wavelength localization of the optical field (i.e. hot spot) [52]. Unfortunately, these sharp features make the optical response of the nanostructure strongly dependent on the resolution and uniformity of the fabrication process [53]. Furthermore, overlapping peaks from tip-localized modes and inhomogeneous broadening due to spatial variations in the dielectric constants of the matrix complicate the interpretation of the optical spectra [38,50]. Nanocrescents pose the additional challenge of having a non-uniform width and thickness, making them difficult to model and difficult to study systematically. The goal of this article is to provide a blueprint for predicting the infrared spectra of plasmonic nanoarcs. The article concludes with a strategy for fine-tuning the *relative* frequencies of the two dominant attenuation peaks in the spectra, e.g. to separate the frequencies by an octave interval.

2. Sample fabrication and characterization methods

Nanorod and nanoarc arrays were fabricated on double-side polished, single-crystal silicon (0.38 mm thick, n-type, 20–30 ohm-cm, Silicon Inc.) and fused quartz substrates (GE124, #26016, 0.5 mm thick, Ted Pella) using electron beam lithography (EBL), followed by thermal evaporation of Au or Al and lift-off. Before patterning, two layers of photoresists, ~100 nm P(MMA (8.5) MAA) (6% in ethyl lactate, MicroChem) and ~80 nm PMMA (950k molecular weight, 2% in anisole, MicroChem), were spin-coated onto the substrate and were baked at 180 °C for 1 min and 10 min, respectively. For quartz substrates, a conductive polymer (aquaSAVE) was spun on top of the bilayer resist. EBL pattering was performed in an Elionix G100 system with an accelerating voltage of 100 kV and an e-beam current of 1 nA. After development in 1:3 methyl isobutyl ketone:isopropanol, a 55 nm thick metal film (gold 99.995% or aluminum 99.999%) was thermally evaporated onto the patterned sample (without adhesion layers). Lift-off was completed by submerging the sample in acetone at room temperature. The nanoarc arrays were each 20×20 μm^2 or 80×80 μm^2 in area. The separation between individual nanoarcs within an array was at least 1.5 times the mid-arc length L_{mid} (see Fig. 1(b) and definition in Section 3.1) in order to prevent spectral shifts due to dipolar coupling between neighboring nanoantennas. This ensures that the spectrum of the array can be used in our analysis in lieu of a spectrum of an individual nanoantenna.

Within each array identical nanostructures were made with nominal lengths in the range of $L = 180$–2170 nm, a constant width of $W = 55 \pm 5$ nm, and a constant thickness of $t = 55$ nm. For nanoarcs, the central angle θ was varied between 0° and 210°, where $\theta = 0°$ corresponds to a nanorod, $\theta = 90°$ corresponds to a quarter of a ring, $\theta = 180°$ corresponds to half a ring, etc. SEM imaging was performed in a Hitachi SU-70 with 10 kV accelerating voltage and 5 mm working distance to determine the physical length L for nanorods, height H for nanoarcs and width W of the nanostructures in each array (see Fig. 1). SEM imaging indicates that the corners of the nanostructures are rounded with a characteristic radius of approx. 10 nm, which has a minor influence on the spectra, according to numerical modeling. The thickness of the nanostructures was measured using an Asylum Research Cypher ES atomic force microscopy (AFM) system in tapping mode.

Infrared reflection and transmission spectra of gold nanoarcs on silicon were acquired with a synchrotron-based system (LBNL ALS beamline 1.4 combined with a Nicolet FTIR spectrometer and a Nicolet Nic-Plan IR microscope). The incident light was focused using a 32x Schwarzschild objective lens onto the center of the nanoarc array. The focused light had a diffraction limited diameter of ~10 μm, illuminating approx. 30 nanoarcs for each measurement. Additional measurements were performed using a Nicolet Continuum IR microscope coupled to a Nicolet iS50 FTIR spectrometer. This benchtop spectrometer employs a tungsten-halogen white light source in the near-IR and a Thermo Scientific Polaris source in the mid-IR. A 15x objective lens and an image-plane aperture were used to selectively probe a single array of nanoarcs. The aperture size was 30×30 μm^2 for small-area arrays, and 70×70 μm^2 for large-area arrays. Spectra were collected in the wavelength range of 1,000–15,350 nm (650–10,000 cm^{-1}) excluding ranges of high attenuation by the substrates. For polarization-dependent FTIR spectroscopy, a wire-grid linear polarizer (WP25M-UB, Thorlabs) was placed between the light source and the sample. Alignment of the polarizer axis with respect to the sample axes was achieved by minimizing the FTIR signal from the fundamental LSPR mode. In all the FTIR measurements light was incident normally on the sample plane and was detected with a liquid nitrogen-cooled mercury cadmium telluride (MCT) detector. These spectroscopic measurements identified one or more LSPRs for each array of nanostructures as peaks in the reflectance spectra and corresponding dips in the transmission spectra. The LSPR wavelengths (λ_{res}) of the nanoarcs are widely tunable throughout the infrared spectral range by adjusting shape parameters (H, W, t or θ) or changing the materials used.

3. Results and discussion

3.1. Transformation optics analysis

To elucidate which nanoarc dimensions are important for controlling the resonance wavelength, we employ the method of transformation optics [54,55] to map a nanoarc into a nanorod (and vice versa) using a two-dimensional (2D) conformal transformation. For isotropic, non-magnetic materials, conformal transformations conserve the in-plane permittivity values [56,57], and as a result the transformed system shares the same longitudinal surface plasmon resonance conditions as the original system. The shape parameters of the nanorod-to-nanoarc transformation (in 2D) are depicted in Fig. 1(c). We map a nanorod of length L and width W to a nanoarc through the conformal transformation [58]

$$z' = \exp(\gamma z) \tag{1}$$

with the usual complex number notations $z = x + iy$ for the original (rod) plane and $z' = x' + iy'$ for the transformed (arc) plane. The parameter γ sets the central angle θ (in radians) subtended by the resulting arc via the relation

$$\gamma = \frac{\theta}{L}, \tag{2}$$

where L is the length of the rod and γ is real. By selecting different values of γ, the same nanorod of length L can be mapped into a set of different nanoarcs with central angle of γL. The parameter γ also sets a periodic boundary condition in the original plane: the permittivity values need to display a periodicity of $2\pi/\gamma$ along the y-axis, $\varepsilon(x, y) = \varepsilon(x, y + 2\pi/\gamma)$, i.e. the nanorod is an element in a one-dimensional (1D) array. The inverse conformal transformation maps any individual nanoarc onto an array of nanorods of dimensions L-by-W if two conditions are satisfied: (I) The origin of the nanoarc radii (i.e., the ring center) is placed at $z' = 0$, such that the coordinates x'_R and x'_L in Fig. 1(c) correspond with the outer and inner radii of the arc, respectively. (II) The nanoarc mid-arc length (L_{mid} in Fig. 1(b)), defined as the length of the line contour stretching along the middle of the width of the arc from one tip to the other, and computed using Eq. (3), and the nanoarc width ($W' = x'_R - x'_L$) relate to L, W and θ according to Eq. (4). To maintain these geometric dimensions within narrow bounds, we chose $L_{mid} = L$ and computed the value for W'. The maximum difference between W and W' in the nanoarc patterns in this work is 3 nm (for $L = 180$ nm and $W = 50$ nm), which is comparable to the length uncertainty in the EBL pattern generation process. For most of our structures $L > 500$ nm, $|W - W'| < 0.5$ nm and this difference is inconsequential. Effectively, the above discussion identifies a conformal transformation that maps a 1D array of rods with length L to an individual

Optics EXPRESS

arc with mid-arc length $L_{mid} = L$, and vice versa, independent of the curvature, with the width and thickness unaltered. Nanoarcs with small central angles ($\theta < 145°$) correspond to nanorod arrays with elements far enough apart that plasmonic coupling between them can be neglected. In this scenario, the transformation optics analysis suggests that nanoarcs with different curvatures share the same LSPR spectra as long as they share the same L_{mid}, W and t. Furthermore, the variation of λ_{res} with L_{mid} in nanoarcs should track the variation of λ_{res} with L in nanorods [28,30,36]. Overall, this analysis suggests that the vast knowledge available for plasmonic nanorods and nanorod arrays can be readily utilized to predict the properties of plasmonic nanoarcs. Care must be taken when the central angle exceeds approximately 145°, since increasing the arc curvature should cause a blue-shift in the fundamental resonance, in line with LSPR spectra of arrays of plasmonic nanorods coupled via short tip-to-tip gap distances (gap < 1.5L) [29,30].

$$L_{mid} = \left(\frac{x'_R + x'_L}{2}\right)\theta \tag{3}$$

$$\frac{\theta W'}{L_{mid}} = 2\left(\frac{\exp(\frac{\theta W}{L}) - 1}{\exp(\frac{\theta W}{L}) + 1}\right) \tag{4}$$

3.2. Nanoarcs with a uniform width profile

The analysis of transformation optics is supported by experimental and simulation-based determination of the LSPR wavelengths of nanoarcs. Figures 2(a) and 2(b) show, respectively, SEM images and the measured unpolarized FTIR transmission (T) spectra of gold nanoarcs on silicon with fixed $L_{mid} = 600$ nm, $W = 55$ nm, $t = 55$ nm, and subtending various central angles ($\theta = 0°$–$180°$). These nanoarcs can be considered as being transformed from the same nanorod element. As predicted by transformation optics, the resonance wavelengths are fixed because L_{mid} is constant, and these wavelengths are insensitive to the central angle of the nanoarcs or the radii of curvature. Specifically, the transmission dips for the 1st and 2nd LSPR modes of the nanorod ($\theta = 0°$) are centered at 3850 nm and 1989 nm, respectively. The resonance wavelength of the 1st mode (λ_1) of the other 13 nanoarcs is found in the range of 3818–3878 nm, and the resonance wavelength of the 2nd mode (λ_2) ranges from 1979 nm to 2007 nm. These wavelength variations are smaller than the shifts attributed to fabrication flaws and sample inhomogeneity (±1.75%) determined independently by the analysis of spectra from nanostructure arrays replicated ~50 times on a single substrate. The ranges of resonance wavelength variation are also significantly narrower than the linewidth of the resonance (~20% λ_{res}). These LSPR wavelength variations are addressed further in the simulations and in the discussion that follows.

The transmission data in Fig. 2(b) shows that while the resonance wavelength does not depend on θ, the resonance intensity varies significantly with θ. The signal intensity depends on the polarizability of the nanoarcs and the relative orientation between the oscillating electric dipole of the resonance mode and the polarization of the light. The attenuation of the nanoarcs is maximized when the polarization of the incident light matches the electric dipole orientation; when the two orientations are orthogonal, the attenuation is zero. In longitudinal LSPR modes of nanoarcs, for which the surface charge density oscillates along a trajectory that tracks the bend of the nanoarc from one tip to the other, two orthogonal electric dipole orientations are possible. The calculated electric field profiles of the LSPR modes of nanoarcs (Fig. 8 in Appendix) are directly related to the oscillating charge accumulation patterns (illustrations in Fig. 2(c)), and show that the 1st and 2nd order modes exhibit dipole moments that are vertically and horizontally oriented, respectively. The orthogonal electric dipoles can be excited separately by probing aligned nanostructures with linearly polarized light. As shown by the spectra and illustrations in Fig. 2(c), y'-linearly polarized light can only excite odd-order modes, while x'-linearly polarized light can only excite even-order modes (x'- and y'-axes as defined in Fig. 1(c)). This agrees with

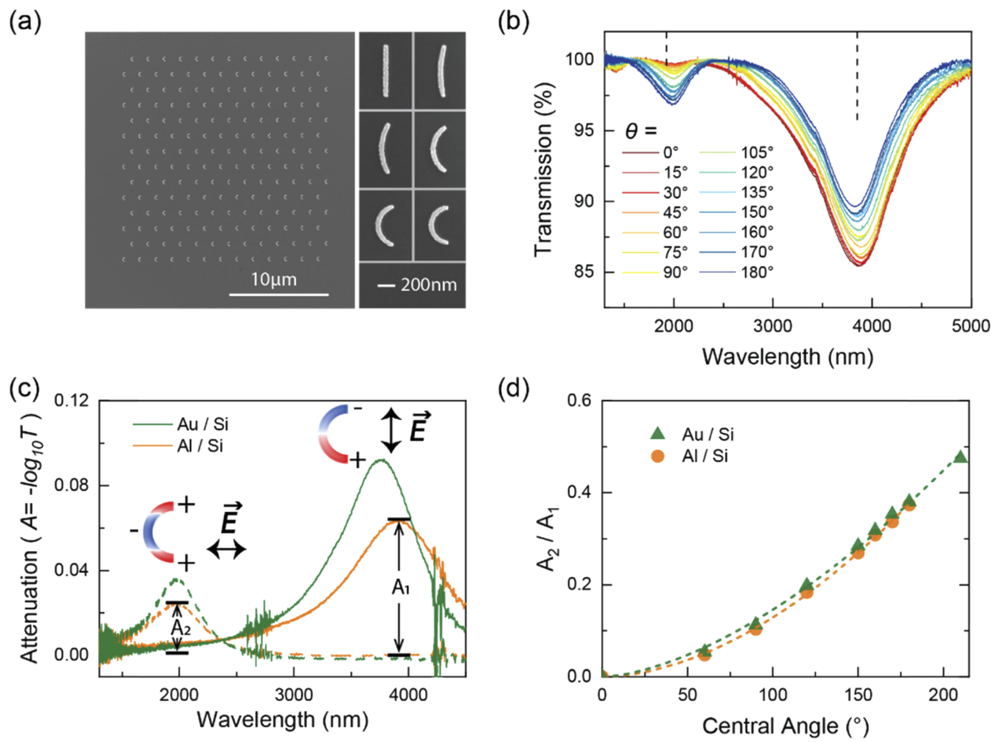

Fig. 2. (a, b) Gold nanoarcs on silicon with $L_{mid} = 600$ nm, $W = 55$ nm and $t = 55$ nm. (a) SEM images of an array of nanoarcs with $\theta = 180°$ (left) and individual nanoarcs with $\theta = 0°$, 30°, 60°, 120°, 150°, 180° (right). (b) Experimental FTIR transmission spectra of the nanoarcs with $\theta = 0°$–180°. The vertical dash lines illustrate an interval of precisely one octave between two wavelengths: λ_1 of the nanoarcs with $\theta = 180°$ at 3818 nm, and $\lambda_1/2$ at 1909 nm. (c) Polarized attenuation spectra of an aluminum nanoarc array on silicon (orange) with $L_{mid} = 730$ nm, $W = 55$ nm, $t = 55$ nm and $\theta = 180°$, and a gold nanoarc array on silicon (green) with $L_{mid} = 600$ nm, $W = 55$ nm, $t = 55$ nm, and $\theta = 180°$. The dashed line data were obtained with *x'*-polarized light and the solid line data were obtained with *y'*-polarized light. The illustrations represent the charge accumulation patterns on the surface of the arc for each of the orthogonal polarizations at resonance. (d) The ratio of the attenuation by the 2nd and 1st LSPRs of gold (green triangles) and aluminum (orange circles) nanoarcs on silicon. The dashed lines are a guide to the eye.

Optics EXPRESS

measurements from split-ring resonators [59], nanocrescents [10,51,52] and V-shaped antennas [17,60] showing that the excitation of the LSPR modes is polarization dependent. Holding L_{mid} constant, as θ increases the polarizability of the 2nd LSPR mode (which is proportional to the on-resonance attenuation) grows, while that of the 1st LSPR mode wanes. The relative strength of the two modes was quantified using polarization-dependent FTIR spectroscopy. These experiments confirmed that the central angle θ is instrumental in tuning the relative strength of the resonances in nanoarcs. We recorded the attenuation ($A = -\ log_{10}T$) spectra for several sets of nanoarcs for which the 1st and 2nd LSPR data could be collected simultaneously and without interference from absorption by the substrate, the atmosphere and the optical setup (Fig. 2(c)). This was accomplished for $\lambda_1 = 4$ µm and $\lambda_2 = 2$ µm for nanoarcs on silicon, and for $\lambda_1 = 2.4$–4.3 µm and $\lambda_2 = 1.2$–2.2 µm for nanoarcs on quartz.

Tracking the peak attenuation by the 1st and 2nd LSPRs ($A_1 = A[\lambda_1]$ and $A_2 = A[\lambda_2]$) as a function of the nanoarc central angle, common trends were found in all the sets of nanoarcs. For the 1st mode, the peak attenuation (A_1) decreases as the central angle of the nanoarc increases. The attenuation by the 2nd mode (A_2) shows the opposite trend. The ratio A_2 / A_1 increases up to a value of 0.38 in the range of central angles from 0° to 180°, and increases further for arcs with larger central angles. These data are shown in Fig. 2(d) for two sets of nanoarcs with similar LSPR spectra ($\lambda_1 = 4$ µm and $\lambda_2 = 2$ µm). The first set consisted of arrays of aluminum nanoarcs on silicon with $L_{mid} = 730$ nm, $W = 60$ nm, $t = 55$ nm ($\theta = 0°$–180°), and the second sets consisted of arrays of gold nanoarcs on silicon with $L_{mid} = 600$ nm, $W = 50$ nm, $t = 55$ nm ($\theta = 0°$–210°). Data from three sets of gold nanoarcs on quartz with $L_{mid} = 600$ nm, 800 nm and 1200 nm ($\theta = 0°$–180°) were indistinguishable from that shown in Fig. 2(d) for nanoarcs on silicon (not shown). Thus, the dependence of A_2 / A_1 on θ appears to be universal for high-aspect ratio nanoarcs of various dimensions and materials. The data indicates that, with two intense LSPR features, nanoarcs subtending large central angles are most promising for observing and enhancing effects that rely on coupling between plasmon modes separated by approximately one octave, such as second harmonic generation. In comparison, with plasmonic nanorods ($\theta = 0°$), the electric dipole moment of the 2nd LSPR mode vanishes due to symmetry, and theoretically it cannot be excited by a plane wave at normal incidence. The 3rd longitudinal LSPR mode in nanorods is substantially weaker than the fundamental mode and is separated from it by approximately one and a half octaves (red curve in Fig. 2(b)). In addition to the 1st and 3rd LSPR mode peaks, in our measurements the nanorod array shows a very weak, yet non-zero, attenuation at the wavelength corresponding to the 2nd LSPR mode. This is attributed to the conical illumination generated by the Schwarzschild objective lens in the experiments and symmetry-breaking defects introduced by imperfect lithography [27,61,62].

Numerical simulations further support the analyses above. The near-field response of plasmonic nanoarcs to electromagnetic radiation was simulated using the finite-difference-time-domain software *Lumerical*, providing data that agrees well with the experimental results and the analysis based on transformation optics. Full details of the simulation methods are provided in the Appendix. The calculated extinction cross-section spectra of gold nanoarcs on quartz with $L_{mid} = 395$ nm and subtending different central angles show two peaks in the near-IR region, centered at $\lambda_1 = 1653$ nm and $\lambda_2 = 920$ nm. The calculated spectra and the extracted λ_1 values are presented in Fig. 3(a) and in Table 1, respectively. These spectra are in good agreement with the experimental spectra of Au arcs on quartz with similar dimensions (Fig. 3(b) and Table 1), and they clearly indicate that (I) the resonance wavelengths of nanoarcs are primarily determined by L_{mid}; and (II) the extinction cross-section decreases for the 1st LSPR mode and increases for the 2nd LSPR mode as the central angle increases from 0° to 180°. Detailed inspection of the calculated values of λ_1 revealed minor but consistent shifts in λ_1 as θ is varied, i.e. the wavelength reaches a maximum value as the central angle approaches 60° and decreases slightly for large central angles. This trend was observed in measured data in several series of samples

Optics EXPRESS

with constant L_{mid}, including in the data in Fig. 2(b), yet in other series this weak effect was masked by statistical deviations in the measurement data (e.g. Table 1 data). The values of λ_2 did not show any notable trend with respect to θ in the simulations nor in the experiments.

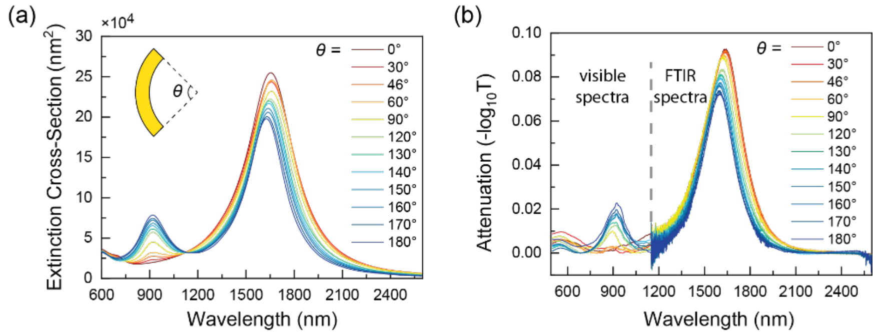

Fig. 3. (a) Calculated extinction cross-section spectra of gold nanoarcs on quartz with $L_{mid} = 395$ nm, $W = 62$ nm, $t = 50$ nm, and $\theta = 0°–180°$. (b) Measured visible and FTIR attenuation spectra of gold nanoarcs on quartz with $L_{mid} = 395$ nm, $W = 60$ nm, $t = 55$ nm, and $\theta = 0°–180°$. The spectra in the visible range were obtained using a microspectrophotometer (Microspectra 121, CRAIC Technologies) in transmission mode.

Table 1. Calculated and measured 1st LSPR wavelength of gold nanoarcs on quartz with $L_{mid} = 395$ nm[a]

θ (°)	0	30	46	60	90	120	140	160	180
Calculated λ_1 (nm)[b]	1653	1657	1660	1660	1657	1653	1643	1639	1626
Measured λ_1 (nm)[c]	1639	1634	1637	1628	1621	1616	1605	1598	1600

[a]In the simulations, $W = 62$ nm and $t = 50$ nm; in the experiments, $W = 60$ nm and $t = 55$ nm (nominal values).
[b]The uncertainty in Calculated λ_1 is ±4 nm due to the discrete frequency grid used in the simulations.
[c]The uncertainty in Measured λ_1 is ±15 nm due to the peak fitting procedure and fabrication flaws in the sample.

Even though transformation optics predicts λ_1 will vary with central angle upon the onset of rod-rod coupling in the original plane, and FTIR spectroscopy on 1D plasmonic nanorod arrays has demonstrated that λ_1 shifts to shorter wavelengths as the unit cell length is reduced to $2.5L$ or below, these shifts should be observed only in the spectra of plasmonic nanoarcs with $\theta > 2\pi/2.5$ (or 144°). The full-wave electromagnetic simulations capture the small shifts in λ_{res} as θ is varied. A justification for the different trends in $\lambda_1(\theta)$ and $\lambda_2(\theta)$ can be found from closer inspection of the simulated LSPR modes (see Appendix). The 1st longitudinal LSPR mode in plasmonic nanoarcs involves an oscillatory electrical current in a curved trajectory from tip to tip. Consequently, at the resonance frequency the mode displays simultaneously an in-plane oscillating electric dipole and an out-of-plane oscillating magnetic dipole [63,64]. In contrast, the 2nd longitudinal LSPR mode has only an electric dipole character. The coupling between the magnetic and electric responses may be responsible for a shift in the resonance λ_1 that intensifies as the curvature increases, without shifting λ_2 [65]. We note that a previous computational study reported on the minor blue-shift in λ_1 as the curvature increases in nanoarcs subtending large central angles, from 90° up to at least 270°, until the onset of capacitive coupling between the tips of the arc dramatically red-shifts the resonance [42].

The dependence of λ_{res} on L_{mid} in nanoarcs was investigated experimentally, using arrays of plasmonic nanoarcs with $L_{mid} = 180–2170$ nm and central angle $\theta = 0°–180°$. Figure 4(a) shows the measured 1st and 2nd resonance wavelengths (λ_1 and λ_2) as a function of L_{mid} for

Research Article Vol. 28, No. 21 / 12 October 2020 / Optics Express 30897

aluminum nanoarcs on quartz. Figure 4(b) shows the corresponding data for gold nanoarcs on silicon. The LSPR data for all the nanoarcs, including all central angles, lines up into a pair of curves. A linear relationship between resonance wavelength λ_{res} and L_{mid} is observed for both the 1st and 2nd LSPR modes. Based on the transformation optics predictions, these linear trends should match the linear trends previously observed in multiple experimental studies of plasmonic nanorods; and the available literature on nanorods can be used to predict the LSPR wavelengths of nanoarcs. The dependence of the resonance wavelength λ_{res} on the nanorod length L is often explained with a model that considers the nanorod as a Fabry-Perot cavity for standing waves of surface plasmons [66,67]. This model results in a linear relationship with the slope

$$\frac{d\lambda_{res}}{dL} = \frac{2n_{eff}(\lambda)}{m}, \tag{5}$$

where n_{eff} is the effective refractive index of the metal-dielectric interface, and m is the order of the longitudinal mode ($m = 1, 2, 3, \ldots$). Predicting the value of n_{eff} with analytic models when the nanorod is placed on a semi-infinite dielectric substrate has been a challenging task [3,28,30,68]. Numerical calculations by Berini [69] showed that the propagation constants of surface plasmon polaritons (SPP) in infinite metal strips on the surface of a semi-infinite dielectric substrate depend not only on the permittivities of the metal, the substrate material and air, but also on the mode order, the width and the thickness of the strip. Berini's calculations that considered strips 500 nm or wider, and thick enough such that the surface plasmon mode is concentrated in the high-permittivity substrate, resulted in n_{eff} values that are not very different from the value derived from the phase constant of the SPP mode supported by the interface between semi-infinite metallic and dielectric regions, as in Eq. (6).

$$n_{eff}(\omega) \approx \frac{\beta_{SPP}}{k_0} = \text{Re}\left[\sqrt{\frac{\varepsilon_M \varepsilon_r}{\varepsilon_M + \varepsilon_r}}\right] \tag{6}$$

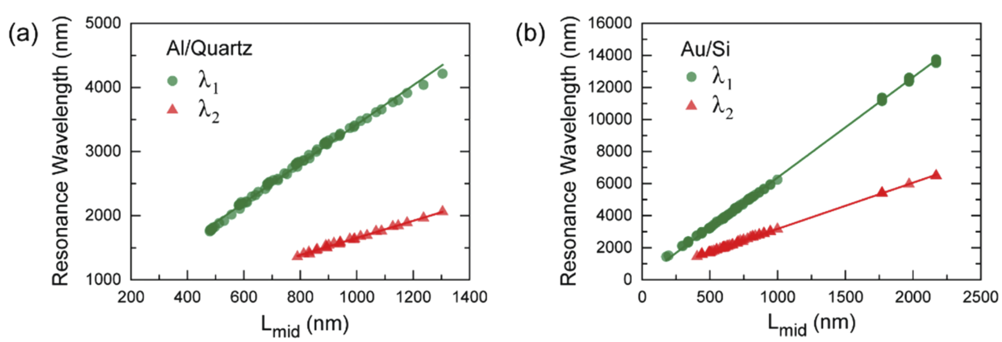

Fig. 4. The 1st (green circles) and 2nd (red triangles) LSPR wavelengths of (a) aluminum nanoarcs on quartz with $L_{mid} = 460$–1300 nm, $W = 60$ nm, $t = 55$ nm and $\theta = 0°$–$180°$, and of (b) gold nanoarcs on silicon with $L_{mid} = 180$–2170 nm, $W = 55$ nm, $t = 55$ nm and $\theta = 0°$–$180°$. Data points obtained from measured FTIR spectra. Solid line is a linear fit for the data in the series. L_{mid} values are nominal values.

In Eq. (6), β_{SPP} is the phase constant of the SPP mode, $k_0 = \omega / c$ is the wavenumber in free space (ω is the frequency and c is the speed of light in vacuum), ε_M is the complex relative permittivity of the metal and ε_r is the relative permittivity of the high index material (i.e. the substrate). Because of the large negative value of Re[ε_M] in the spectral range of interest, the right-hand side in Eq. (6) simplifies to $\sqrt{\varepsilon_r}$. This value is used here as a guiding approximation. Berini's model predicts that for the longitudinal surface plasmon modes n_{eff} may increase from this value as the width and thickness of the metal strip are reduced. For quartz, $\sqrt{\varepsilon_r}$=1.46. For silicon, $\sqrt{\varepsilon_r}$=3.44, however, the presence of a 7 nm native oxide film at the interface prevents intimate contact between the gold and the silicon, and lowers the value of n_{eff} significantly. The value of the slope of the linear fit in Fig. 4(a) is 3.06 ± 0.03 for the long wavelength mode ($m = 1$) and 1.34 ± 0.02 for the short wavelength mode ($m = 2$). The value of the slope in Fig. 4(b) is 6.27 ± 0.01 for the long wavelength mode and 2.89 ± 0.01 for the short wavelength mode. Notably, the ratio of the slopes is close but not equal to 2 as would be predicted by Eq. (5), and neither of the linear fits passes through the origin. The interval between the frequencies of the modes is not fixed, and is equal to an octave (λ_1 / $\lambda_2 = 2$) only at a single value of L_{mid} that is material dependent. In our experiments, the slope clearly increased when choosing a higher index substrate, in line with Eqs. (5) and (6). Changing the metal did not significantly affect the slope value. Switching the metal from gold to aluminum shifted the resonances to shorter wavelengths by approximately a constant $\Delta\lambda_{res}$.

The dependence of λ_1 on L_{mid} in nanoarcs can be discerned reliably from data for nanorods. When considering only the data for nanorods ($\theta = 0°$) in Fig. 4(b), the linear fit gives the empirical relation $\lambda_1 = 6.31 \times L$+80 nm for nanorods with lengths ranging from 440 nm to 2170 nm. The value of λ_1 for the nanoarcs of all central angles can be predicted using this linear relation by setting $L = L_{mid}$. A comparison between the measured λ_1 values and the predicted values shows an average difference of 0.75% and a maximum difference of 2.4%. No similar strategy to predict the values of λ_2 in nanoarcs from data for nanorods can be implemented, since even-order modes in nanorods do not couple to radiation.

Briefly, we note that the dipolar coupling between neighboring nanoarcs in periodic arrays of the nanostructures was investigated by varying the lattice parameters of the array. The effect of dipolar coupling in nanoarcs is to shift the fundamental LSPR to shorter wavelengths regardless of the orientation of the position-vector connecting the interacting nanostructures, as reported previously for nanorods [30,68].

The FTIR spectra also contain signals that originate from the substrate (Fig. 5). In the case of silicon substrates, weak signals are observed at 1100 cm^{-1} and 1250 cm^{-1} associated with optical absorption by surface phonons of the thin native oxide layer and Si-O bond vibrations [70]. When an LSPR mode of a gold nanoarc spectrally overlaps with a substrate signal, strong coupling between the surface plasmons and the phonons (vibrations) occurs, as indicated by the emergence of phonon (vibration)-induced transparency [71,72]. This coupling is strongly evident in the spectra of gold nanoarcs on silicon with $\lambda_1 = 7.4$–10.5 µm (corresponding to $L_{mid} = 1200$–1700 nm) where the absorption peak shape is distorted, and therefore not reported in Fig. 4(b). In Fig. 5(a), representative spectra illustrate the effect. The attenuation by SiO_x, typically reducing the transmission by 0.4%T, is enhanced to ~2%T by an off-resonance interaction with the surface plasmons of an Au nanoarc with $L_{mid} = 910$ nm; whereas the on-resonance interaction with an $L_{mid} = 1550$ nm nanoarc leads to an apparent reduction of the plasmon absorption, adding more than 5%T to the recorded transmission. Notably, the magnitude of the transparency effect, measured as the difference in the LSPR absorption with and without coupling to the substrate, is 1–3 orders of magnitude larger than the attenuation of the pure substrate, providing a mechanism for enhanced chemical sensing of near-surface structures akin surface enhanced IR absorption (SEIRA) and surface enhance Raman scattering (SERS). For example, vibration-induced transparency at 1734 cm^{-1} was used to assess the presence of residual PMMA during the processing of the samples for this work.

3.3. Nanoarcs with a non-uniform width profile

There is a growing interest in the application of plasmonic nanostructures in non-linear optics. Plasmonic SRRs have been used for second- and third- harmonic generation (SHG, THG) to convert IR optical signals to visible light [75,76]. An improvement in the SHG efficiency could

Optics EXPRESS

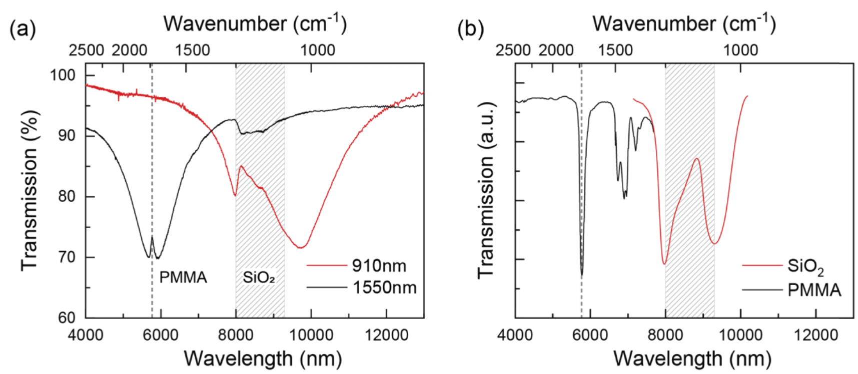

Fig. 5. (a) FTIR transmission spectra of gold nanoarcs on silicon with $L_{mid} = 910$ nm (black) or 1550 nm (red). The black line was shifted by -6% for clarity. (b) Transmission spectra of PMMA (black curve, adapted from Ref. [73]) and oblique-incidence transmission spectra of amorphous silicon dioxide (red curve, adapted from Ref. [74]). The gray dashed lines mark the position of the C = O vibrational band of PMMA. The shaded areas denote the relevant IR band of the bulk and surface phonon modes of silicon dioxide.

be achieved if the resonances of the nano-antenna occurred at both the fundamental and second harmonic wavelengths, i.e. $\lambda_1 / s\lambda_2 = 2$ [60]. Yet, this condition is not automatically satisfied for SRRs nor for nanoarcs (see Fig. 2(b)). The data collected in this work shows that the ratio λ_1 / λ_2 for nanoarcs increases as L_{mid} increases. For gold nanoarcs fabricated on silicon, λ_1 / λ_2 increases from 1.83 to 2.09 as L_{mid} increases from 440 nm to 2170 nm. For aluminum nanoarcs on quartz with $L_{mid} = 760$–1300 nm, the range of λ_1 / λ_2 is 2.03–2.08. Therefore, a strategy is needed to tune the resonance frequency of each mode independently without resorting to challenging designs such as multimers separated by few-nm gaps [60,77,78]. The transverse dimension of the metal strip, i.e. the width W, is an independent parameter permitting further tuning of the resonances. We have investigated how the LSPR wavelengths change when the metal strip width is modified selectively at the nanoarc tips and at the nanoarc center, where the surface plasmon charge density accumulates at resonance.

Nanoarcs with a non-uniform width profile were designed by applying the geometric transformation of Eqs. (1) and (2) to nanorods with a non-uniform width profile. For these nanorods, we have set the parameters length L, width at tips W_{tip}, and width at center W_{mid}, as shown in Fig. 6. The smooth contour along the long edges of the nanorod was obtained by defining the position-dependent width of the nanorod as $W(y) = W_{mid} + 2\delta\sin^2(\pi y/L)$ (Fig. 6(a)) or $W(y) = W_{tip} + 2\delta\cos^2(\pi y/L)$ (Fig. 6(b)), where δ is the amplitude ($|2\delta| = |W_{mid}\text{-}W_{tip}|$) and L is the length of the rod. W_{mid} can be wider or narrower than W_{tip} depending on the sign of δ; both instances were investigated. The non-uniform nanorods were transformed to nanoarcs (Figs. 6(c) and (d)). With the appropriate choice of x_L and x_R, W_{mid} of the nanoarc is identical to that of the corresponding nanorod, while W_{tip} of the transformed nanoarc and the original nanorod are slightly different. However, the difference (<1.2 nm in our design) is below the resolution of EBL patterning.

For nanoarcs with fixed L, t, W_{mid} and θ, as W_{tip} increases λ_1 red-shifts and, to a lesser extent, λ_2 blue-shifts. For nanoarcs with fixed L, t, W_{tip} and θ, as W_{mid} increases λ_1 blue-shifts, and so does λ_2–but by an order of magnitude less. Figure 7(a) shows an example of this behavior, by overlaying the measured transmission spectra of gold nanoarcs on silicon with $L = 600$ nm, $t = 55$ nm, $W_{mid} = 50$ nm, $\theta = 180°$ and various W_{tip} values (40–110 nm). As W_{tip} increases, λ_1 red-shifts by 634 nm (from 3636 nm to 4720 nm) while λ_2 blue-shifts by 38 nm (from 1978 nm to 1940 nm). As a result, the ratio λ_1 / λ_2 increases from 1.84 to 2.20. Additionally, as W_{tip}

Optics EXPRESS

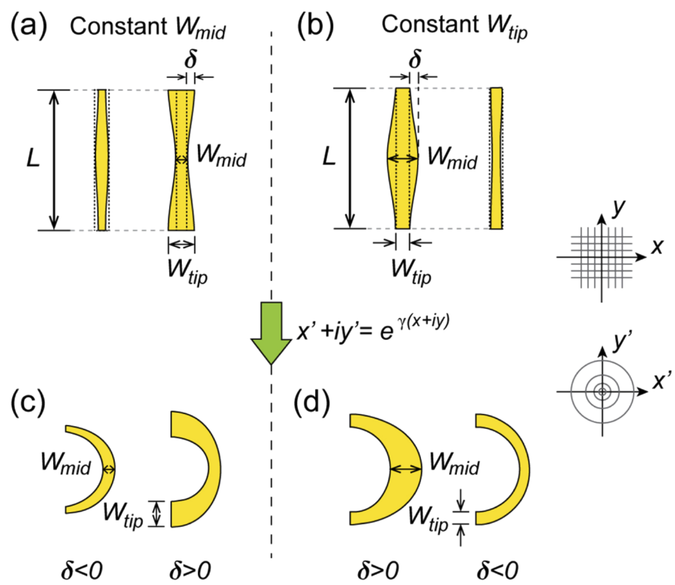

Fig. 6. Designing nanoarcs with a non-uniform width profile. (a, b) Nanorods with a non-uniform width are designed by setting the width at the tips $W_{tip} \equiv W\,(y = \pm L/2)$ and the width at the center $W_{mid} \equiv W\,(y = 0)$ to different values, and creating a smooth width profile from tip to tip as $W(y) = W_{mid} + 2\delta\sin^2(\pi y/L)$ or $W(y) = W_{tip} + 2\delta\cos^2(\pi y/L)$. The width profile of a uniform-width rod ($\delta = 0$) is indicated by the dotted lines. (c, d) The non-uniform nanoarcs are obtained through the conformal transformation of non-uniform nanorods.

increases, the attenuation by the fundamental LSPR mode of the arc increases. Interestingly, varying W_{mid} has no effect on the attenuation. Figure 7(b) shows the dependence of the ratio λ_1

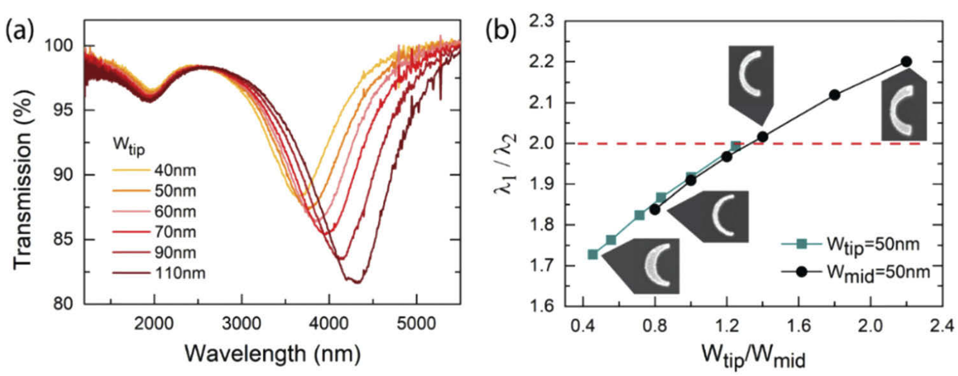

Fig. 7. Resonance tunability in gold nanoarcs on silicon with a non-uniform arc width. (a) Measured FTIR transmission spectra of nanoarcs with $W_{mid} = 50$ nm and $W_{tip} = 40$–110 nm. These nanoarcs were transformed from nanorods with $L = 600$ nm. The central angle $\theta = 180°$. (b) The ratio between the 1st and 2nd resonance wavelengths (λ_1/λ_2) as a function of the ratio between W_{tip} and W_{mid}. Two sets of data are shown here. The set "$W_{mid} = 50$ nm" are data obtained from (a). The set "$W_{tip} = 50$ nm" are data obtained from the spectra of nanoarcs with $W_{mid} = 40$–110 nm and $W_{tip} = 50$ nm. Solid lines are a guide for the eye. The 4 insets are sample SEM images of the nanoarcs corresponding to the indicated data points. The horizontal dashed line marks the octave interval condition.

/ λ_2 on W_{tip} (black circles) and on W_{mid} (green squares). Both width parameters are effective at adjusting the interval between the resonances. The overlap between the datasets in Fig. 7(b) indicates that W_{tip} / W_{mid} is a dominant parameter in determining the ratio λ_1 / λ_2 of the nanoarcs. For both series, the ratio λ_1 / λ_2 acquires the value of 2 when W_{tip} / W_{mid} is set to 1.25–1.30. The features of Fig. 7(b) are unchanged when analyzing nanoarcs with other central angles ($\theta < 180°$). When analyzing nanoarcs with other values of L or made of other materials, the trends remain the same: there is a monotonic dependence of λ_1 / λ_2 on W_{tip} / W_{mid} in nanoarcs; the particular values of the ratio λ_1 / λ_2 often increase with L and vary from material to material. The design of nanoarcs with a non-uniform width profile to finely tune the 1st and 2nd longitudinal LSPR resonances and their interval was thus confirmed to have broad applicability across the near- and mid-IR.

4. Conclusions

We investigated the LSPR wavelengths of nanoarcs with uniform and non-uniform width. Using a 2D conformal transformation, we mapped nanorods into nanoarcs ($0° \leq \theta \leq 180°$). The two types of nanostructures share the same LSPR wavelengths and thus the well-studied plasmonic characteristics of nanorods can be directly applied to predict the behavior of nanoarcs. With the experimental and numerical simulation results, we have shown that L_{mid} is an effective length that determines the LSPR wavelengths of nanoarcs with uniform width. The linear dependence of the LSPR wavelength on the length of the nanorod $\lambda_1 = aL + b$ applies with the same slope and intercept values to nanoarcs using the mid-arc length $\lambda_1 = aL_{mid} + b$. The fundamental LSPR wavelength of nanoarcs with uniform width can be tuned predictably in the NIR and MIR regimes (1.5–13.6 µm, or 730–6500 cm^{-1}). Adjusting the central angle of the nanoarc has a minor effect on the LSPR wavelength, but it changes the attenuation by different-order LSPR modes. The attenuation by the 1st LSPR mode decreases as the central angle increases while the attenuation at the 2nd LSPR mode increases. In addition, we found that for nanoarcs with non-uniform width, the ratio λ_1 / λ_2 can be tuned from 1.73 to 2.20 by varying W_{tip} / W_{mid}. The ability to tune different-order LSPR wavelengths and intensities independently paves the way for nanoarcs to be more widely applied as components for photonic technologies and nonlinear optical devices.

Appendix

Calculation of LSPR wavelengths of nanoarcs

Numerical calculations were performed using 3D finite-difference-time-domain (FDTD) simulations with the *Lumerical* software package (v8.21.1882). The model used in each simulation consisted of a single nanoarc placed on the surface of a semi-infinite substrate. The nanoarc was illuminated by a plane wave. The light scattering and absorption by the nanoarc were monitored while sweeping the excitation wavelength. The electric near-field distributions at resonance conditions were also calculated. We have chosen to address exclusively gold nanoarcs on quartz substrates in order to circumvent including a surface oxide layer at the interface, as would be needed in a model that includes nanoscale objects made of Al or Si.

The simulation region with volume V_{sim} consisted of a single Au nanoarc with a width of $W = 62$ or 40 nm and a thickness of $t = 50$ or 20 nm placed on the surface of a semi-infinite SiO_2 substrate. The mesh size within the volume V_{sim} was set to 2×2×2 nm^3. A perfectly matched layer (PML) boundary condition was applied to all sides of the simulation region in order to minimize Fresnel reflections into the simulation space. The scattering cross-section σ_{scat} and the absorption cross-section σ_{abs} of an isolated nanoarc as a function of frequency–quantities that are parallel to the plasmon attenuation spectrum–were calculated using the Huygens surface method [79] which is also referred to as the total-field-scattered-field (TFSF) method [80]. In the TFSF method, the investigated plasmonic nanoarc is placed inside a TFSF source, a near-field rectangular volume V_{source} contained within the simulation region V_{sim} with boundary electric and magnetic current sheets chosen to produce a normally incident plane wave in the interior of V_{source}, but to cancel the incident, transmitted and reflected plane waves in the exterior of V_{source}. Therefore, the nanoarc responds as if it is excited by a plane wave while the regions exterior to V_{source} contain only the portion of light that was scattered by the nanoarc. In these simulations, the TFSF plane wave propagated towards the substrate surface and the nanoarc at normal incidence (its propagation direction defined as the negative z'-direction) and was linearly polarized with the electric field component oriented 45° with respect to the x'-axis of the nanoarc (same x'-axis as defined in Fig. 1(c)). The scattering cross-section σ_{scat} was defined as $P_{scat} = \sigma_{scat} I$, where I is the intensity given by the magnitude of the time-averaged Poynting vector of the excitation source and P_{scat} is the scattered power calculated as $P_{scat} = \oint \vec{S}_{\text{avg}} \cdot d\vec{A}$, where $\vec{S}_{\text{avg}}$ is the time-averaged Poynting vector of the scattered field outside of V_{source} and the numerical integration was performed over a closed area with surface elements $d\vec{A}$ and enclosing a volume $V_{scat-monitor}$ that contained both the nanoarc and the TFSF source ($V_{source} < V_{scat-monitor} < V_{sim}$). Similarly, the absorption cross-section σ_{abs} was defined as $P_{abs} = \sigma_{abs} I$, where P_{abs} is the power removed from the incident plane wave by absorption, calculated using six rectangular surface monitors enclosing the nanoarc and a volume $V_{abs-monitor}$ within the TFSF source ($V_{abs-monitor} < V_{source} < V_{sim}$). The extinction cross-section was defined as the sum of the scattering and absorption cross-sections, $\sigma_{ext} = \sigma_{scat} + \sigma_{abs}$. The dielectric properties of the gold used in the simulations were taken from independent ellipsometry measurements from a 90-nm thick Au film thermally evaporated on a quartz substrate. A refractive index of 1.45 is used for the SiO_2 substrate [81].

The dependence of the scattering cross-section spectra $\sigma_{scat}(\lambda)$, the absorption cross-section spectra $\sigma_{abs}(\lambda)$ and the extinction spectra $\sigma_{ext}(\lambda)$ on the central angle subtended by the nanoarc was studied in simulations of gold nanoarcs with mid-arc length $L_{mid} = 395$ nm, width $W = 62$ nm, thickness $t = 50$ nm and central angles in the range of $\theta = 0$–180° on quartz substrates. The absorption, scattering and extinction cross-section spectra were calculated over the wavelength range of 600–2600 nm to discern the position and intensity of the fundamental and 2$^{\text{nd}}$ order LSPR peaks. The simulation results were analyzed with respect to experimental FTIR and visible transmission spectra collected from gold nanoarcs with similar dimensions ($L_{mid} = 395$ nm, $W = 60$ nm, $t = 55$ nm, and $\theta = 0°$–180°) fabricated on a fused quartz substrate. The principal results (extinction cross-section spectra and peak wavelengths) were provided in the main text in Fig. 3(a) and Table 1. The scattering cross-section spectra and the absorption cross-section spectra display two peaks at 1626–1664 nm and 913–930 nm [65]. The main difference between the two sets of spectra is in the intensity of the peaks. The values of the scattering cross-section are larger than the values of the absorption cross-section, approximately by up to a factor of 3. At the fundamental resonance wavelength, the intensity of the scattering cross-section decreases with central angle, as was observed in experimental data of nanoarc light attenuation. In contrast, the intensity of the absorption cross-section increases with central angle. Thus, the simulations indicate that in these gold nanoarcs the dominant light-surface plasmon interaction is light scattering. The sum of the scattering and absorption cross-section adequately predicts the wavelength and intensity of the attenuation peaks due to the longitudinal LSPRs in nanoarcs, including the impact of the central angle on these properties. For this reason, the main text delves predominantly on the features of the extinction cross-section (see Fig. 3, Table 1 and related discussion).

The electric near-field distribution around a gold nanoarc on a quartz substrate was simulated for a nanoarc with a mid-arc length of 395 nm and subtending a central angle of 90°. The nanoarc width ($W = 40$ nm) and thickness ($t = 20$ nm) in these simulations were selected to be smaller than the experimental values, as a means of reducing the calculation time while still

Optics EXPRESS

achieving the goals of this investigation. First, a coarse-grid scattering cross-section spectrum was simulated, in order to identify the wavelengths of the LSPR peaks. For this geometry, the resonances occur at $\lambda_1 \approx 2200$ nm and at $\lambda_2 \approx 1100$ nm. At these wavelengths, the electric field distribution within the simulation volume $\bar{E}(\bar{r})$ was calculated and normalized to the magnitude of the electric field of the incident plane wave $|E_0|$. The normalized electric near-field vector field at each resonance condition was analyzed to extract the orientation of the electric dipole, the location of field enhancement sites and their relative enhancement efficiency. Figure 8 shows two profiles of the calculated electric field amplitude in the vicinity of the nanoarc at resonance. The data corresponds to a plane normal to the z'-axis situated in air, 2 nm above the gold surface. The in-plane components of the normalized electric field, E_x / $|E_0|$ and E_y / $|E_0|$, are represented by the arrows, whereas the out-of-plane component E_z / $|E_0|$ is represented by color. In the left panel of Fig. 8, corresponding to the 1st LSPR mode of the nanoarc, the maxima in the electric field amplitude are found at the tips of the nanoarc. The electric field distribution (and the surface charge density) is anti-symmetric with respect to the x'-axis, suggesting an LSPR mode with an instantaneous electric dipole oriented parallel to the y'-axis (and an out-of-plane magnetic dipole, not shown). The electric field intensity is largest at the corners of the arc tips due to the lighting-rod effect and the field enhancement factor $(|E_x|^2 + |E_y|^2 + |E_z|^2) / |E_0|^2$ is up to 4.0×10^3. This strong electric field at the tips of the nanoarc is beneficial for surface enhancement effects including SERS and SERIA. The right panel of Fig. 8 corresponds to the 2nd LSPR mode of the nanoarc. Here, the electric field distribution is symmetric with respect to the x'-axis. For the 2nd LSPR mode, the electric field intensity (and the surface charge density) is high at the two arc tips and around the middle of the arc, with an enhancement factor $(|E_x|^2 + |E_y|^2 + |E_z|^2) / |E_0|^2$ of up to 170, showing additional potential for surface enhanced spectroscopy applications. The centers of mass of the instantaneous positive and negative surface charge are offset, suggesting a mode with an instantaneous electric dipole parallel to the x'-axis, which increases with central angle. The simulation results thus concur that the electric dipoles of the 1st and 2nd LSPR modes are orthogonal to each other. The two modes could therefore be excited individually by y'- or x'-linearly polarized light. This attribute of the resonance modes was utilized in the design of the polarization-dependent spectroscopy measurements reported in the main text.

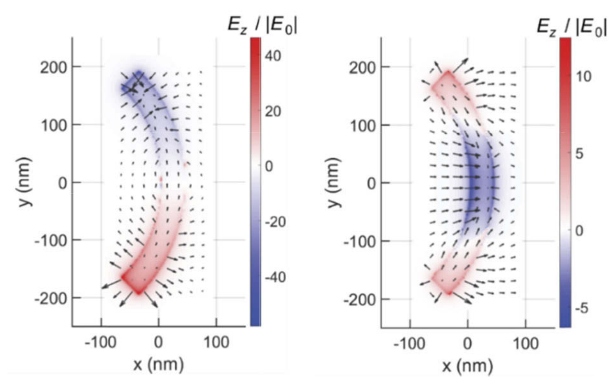

Fig. 8. Calculated surface plasmon mode profiles displayed as the magnitude of the E-field components, in the vicinity of an $L_{mid} = 395$ nm, $W = 40$ nm, $t = 20$ nm, $\theta = 90°$ gold nanoarc on quartz, for excitation wavelengths $\lambda = 2200$ nm (left) and $\lambda = 1100$ nm (right). Arrows represent the normalized in-plane components (E_x / $|E_0|$, E_y / $|E_0|$) of the electric field. Color represent the normalized out-of-plane component (E_z / $|E_0|$) of the electric field. $|E_0|$ is the magnitude of the incident E-field.

Optics EXPRESS

Funding

National Science Foundation (DMR-1151614); University of Maryland (Maryland Catalyst Fund); Office of Naval Research.

Acknowledgements

We thank Prof. Isaak Mayergoyz, Prof. Mohamad Al-Sheikhly, Dr. Zois Tsinas, Dr. Augustine Urbas, Dr. Ekaterina Poutrina and Prof. Sir John Pendry for valuable discussions. This research used resources of the LBNL Advanced Light Source, a User Facility supported by the Office of Science of the U.S. Department of Energy under Contract No. DE-AC02-05CH11231. We acknowledge the support of the Maryland NanoCenter and its AIMLab. We thank the Materials and Manufacturing Directorate at AFRL (Dayton, OH) for use of the microspectrophotometer.

Disclosures

The authors declare no conflicts of interest.

References

1. F. Neubrech, C. Huck, K. Weber, A. Pucci, and H. Giessen, "Surface-Enhanced Infrared Spectroscopy Using Resonant Nanoantennas," Chem. Rev. **117**(7), 5110–5145 (2017).
2. K. A. Willets and R. P. Van Duyne, "Localized surface plasmon resonance spectroscopy and sensing," Annu. Rev. Phys. Chem. **58**(1), 267–297 (2007).
3. K. M. Mayer and J. H. Hafner, "Localized surface plasmon resonance sensors," Chem. Rev. **111**(6), 3828–3857 (2011).
4. W. L. Barnes, A. Dereux, and T. W. Ebbesen, "Surface plasmon subwavelength optics," Nature **424**(6950), 824–830 (2003).
5. E. Ozbay, "Plasmonics: merging photonics and electronics at nanoscale dimensions," Science **311**(5758), 189–193 (2006).
6. A. V. Kabashin, P. Evans, S. Pastkovsky, W. Hendren, G. A. Wurtz, R. Atkinson, R. Pollard, V. A. Podolskiy, and A. V. Zayats, "Plasmonic nanorod metamaterials for biosensing," Nat. Mater. **8**(11), 867–871 (2009).
7. T. K. Sau and C. J. Murphy, "Seeded high yield synthesis of short Au nanorods in aqueous solution," Langmuir **20**(15), 6414–6420 (2004).
8. G. W. Bryant, F. J. Garcia de Abajo, and J. Aizpurua, "Mapping the plasmon resonances of metallic nanoantennas," Nano Lett. **8**(2), 631–636 (2008).
9. I. Zoric, M. Zach, B. Kasemo, and C. Langhammer, "Gold, platinum, and aluminum nanodisk plasmons: material independence, subradiance, and damping mechanisms," ACS Nano **5**(4), 2535–2546 (2011).
10. J. S. Shumaker-Parry, H. Rochholz, and M. Kreiter, "Fabrication of crescent-shaped optical antennas," Adv. Mater. **17**(17), 2131–2134 (2005).
11. L. Y. Wu, B. M. Ross, and L. P. Lee, "Optical properties of the crescent-shaped nanohole antenna," Nano Lett. **9**(5), 1956–1961 (2009).
12. A. W. Clark, A. K. Sheridan, A. Glidle, D. R. S. Cumming, and J. M. Cooper, "Tuneable visible resonances in crescent shaped nano-split-ring resonators," Appl. Phys. Lett. **91**(9), 093109 (2007).
13. M. W. Klein, C. Enkrich, M. Wegener, and S. Linden, "Second-harmonic generation from magnetic metamaterials," Science **313**(5786), 502–504 (2006).
14. R. Marques, J. Martel, F. Mesa, and F. Medina, "Left-handed-media simulation and transmission of EM waves in subwavelength split-ring-resonator-loaded metallic waveguides," Phys. Rev. Lett. **89**(18), 183901 (2002).
15. F. B. P. Niesler, N. Feth, S. Linden, and M. Wegener, "Second-harmonic optical spectroscopy on split-ring-resonator arrays," Opt. Lett. **36**(9), 1533–1535 (2011).
16. C. Rockstuhl, F. Lederer, C. Etrich, T. Zentgraf, J. Kuhl, and H. Giessen, "On the reinterpretation of resonances in split-ring-resonators at normal incidence," Opt. Express **14**(19), 8827–8836 (2006).
17. R. Czaplicki, H. Husu, R. Siikanen, J. Mäkitalo, M. Kauranen, J. Laukkanen, J. Lehtolahti, and M. Kuittinen, "Enhancement of second-harmonic generation from metal nanoparticles by passive elements," Phys. Rev. Lett. **110**(9), 093902 (2013).
18. J. Lee, M. Tymchenko, C. Argyropoulos, P.-Y. Chen, F. Lu, F. Demmerle, G. Boehm, M.-C. Amann, A. Alu, and M. A. Belkin, "Giant nonlinear response from plasmonic metasurfaces coupled to intersubband transitions," Nature **511**(7507), 65–69 (2014).
19. C. Ciracì, E. Poutrina, M. Scalora, and D. R. Smith, "Second-harmonic generation in metallic nanoparticles: Clarification of the role of the surface," Phys. Rev. B **86**(11), 115451 (2012).
20. C. Yi, P. D. Dongare, M.-N. Su, W. Wang, D. Chakraborty, F. Wen, W.-S. Chang, J. E. Sader, P. Nordlander, and N. J. Halas, "Vibrational coupling in plasmonic molecules," Proc. Natl. Acad. Sci. U. S. A. **114**(44), 11621–11626 (2017).

21. M. Decker, M. Ruther, C. E. Kriegler, J. Zhou, C. M. Soukoulis, S. Linden, and M. Wegener, "Strong optical activity from twisted-cross photonic metamaterials," Opt. Lett. **34**(16), 2501–2503 (2009).
22. M. Schnell, P. Sarriugarte, T. Neuman, A. B. Khanikaev, G. Shvets, J. Aizpurua, and R. Hillenbrand, "Real-space mapping of the chiral near-field distributions in spiral antennas and planar metasurfaces," Nano Lett. **16**(1), 663–670 (2016).
23. S. E. Lohse and C. J. Murphy, "The quest for shape control: a history of gold nanorod synthesis," Chem. Mater. **25**(8), 1250–1261 (2013).
24. X. Ye, L. Jin, H. Caglayan, J. Chen, G. Xing, C. Zheng, V. Doan-Nguyen, Y. Kang, N. Engheta, and C. R. Kagan, "Improved size-tunable synthesis of monodisperse gold nanorods through the use of aromatic additives," ACS Nano **6**(3), 2804–2817 (2012).
25. N. R. Jana, L. Gearheart, and C. J. Murphy, "Wet chemical synthesis of high aspect ratio cylindrical gold nanorods," J. Phys. Chem. B **105**(19), 4065–4067 (2001).
26. J. R. Krenn, G. Schider, W. Rechberger, B. Lamprecht, A. Leitner, F. R. Aussenegg, and J. C. Weeber, "Design of multipolar plasmon excitations in silver nanoparticles," Appl. Phys. Lett. **77**(21), 3379–3381 (2000).
27. G. Schider, J. R. Krenn, A. Hohenau, H. Ditlbacher, A. Leitner, F. R. Aussenegg, W. L. Schaich, I. Puscasu, B. Monacelli, and G. Boreman, "Plasmon dispersion relation of Au and Ag nanowires," Phys. Rev. B **68**(15), 155427 (2003).
28. F. Neubrech, T. Kolb, R. Lovrincic, G. Fahsold, A. Pucci, J. Aizpurua, T. W. Cornelius, M. E. Toimil-Molares, R. Neumann, and S. Karim, "Resonances of individual metal nanowires in the infrared," Appl. Phys. Lett. **89**(25), 253104 (2006).
29. R. Adato, A. A. Yanik, C.-H. Wu, G. Shvets, and H. Altug, "Radiative engineering of plasmon lifetimes in embedded nanoantenna arrays," Opt. Express **18**(5), 4526–4537 (2010).
30. B. S. Simpkins, J. P. Long, O. J. Glembocki, J. Guo, J. D. Caldwell, and J. C. Owrutsky, "Pitch-dependent resonances and near-field coupling in infrared nanoantenna arrays," Opt. Express **20**(25), 27725–27739 (2012).
31. F. Neubrech, D. Weber, R. Lovrincic, A. Pucci, M. Lopes, T. Toury, and M. L. de La Chapelle, "Resonances of individual lithographic gold nanowires in the infrared," Appl. Phys. Lett. **93**(16), 163105 (2008).
32. B. Nikoobakht and M. A. El-Sayed, "Preparation and Growth Mechanism of Gold Nanorods (NRs) Using Seed-Mediated Growth Method," Chem. Mater. **15**(10), 1957–1962 (2003).
33. S. Zhang, Z. Ye, Y. Wang, Y. Park, G. Bartal, M. Mrejen, X. Yin, and X. Zhang, "Anti-Hermitian Plasmon Coupling of an Array of Gold Thin-Film Antennas for Controlling Light at the Nanoscale," Phys. Rev. Lett. **109**(19), 193902 (2012).
34. S. T. Shibu Joseph, B. I. Ipe, P. Pramod, and K. G. Thomas, "Gold Nanorods to Nanochains: Mechanistic Investigations on Their Longitudinal Assembly Using α,ω-Alkanedithiols and Interplasmon Coupling," J. Phys. Chem. B **110**(1), 150–157 (2006).
35. J. Yao, Z. Liu, Y. Liu, Y. Wang, C. Sun, G. Bartal, A. M. Stacy, and X. Zhang, "Optical Negative Refraction in Bulk Metamaterials of Nanowires," Science **321**(5891), 930 (2008).
36. R. Adato, A. A. Yanik, J. J. Amsden, D. L. Kaplan, F. G. Omenetto, M. K. Hong, S. Erramilli, and H. Altug, "Ultra-sensitive vibrational spectroscopy of protein monolayers with plasmonic nanoantenna arrays," Proc. Natl. Acad. Sci. U. S. A. **106**(46), 19227–19232 (2009).
37. S.-S. Chang, C.-W. Shih, C.-D. Chen, W.-C. Lai, and C. R. C. Wang, "The Shape Transition of Gold Nanorods," Langmuir **15**(3), 701–709 (1999).
38. L.-J. Black, Y. Wang, C. H. de Groot, A. Arbouet, and O. L. Muskens, "Optimal Polarization Conversion in Coupled Dimer Plasmonic Nanoantennas for Metasurfaces," ACS Nano **8**(6), 6390–6399 (2014).
39. M. Zeisberger, H. Schneidewind, U. Huebner, J. Popp, and M. A. Schmidt, "Nanoboomerang-based inverse metasurfaces—A promising path towards ultrathin photonic devices for transmission operation," APL Photonics **2**(3), 036102 (2017).
40. T. Coenen, F. Bernal Arango, A. Femius Koenderink, and A. Polman, "Directional emission from a single plasmonic scatterer," Nat. Commun. **5**(1), 3250 (2014).
41. G. Lu, Y. Wang, R. Y. Chou, H. Shen, Y. He, Y. Cheng, and Q. Gong, "Directional side scattering of light by a single plasmonic trimer: Directional side scattering of light by a single plasmonic trimer," Laser Photonics Rev. **9**(5), 530–537 (2015).
42. A. Pors, M. Willatzen, O. Albrektsen, and S. I. Bozhevolnyi, "From plasmonic nanoantennas to split-ring resonators: tuning scattering strength," J. Opt. Soc. Am. B **27**(8), 1680–1687 (2010).
43. F. Monticone and A. Alù, "The quest for optical magnetism: from split-ring resonators to plasmonic nanoparticles and nanoclusters," J. Mater. Chem. C **2**(43), 9059–9072 (2014).
44. S. M. Hein and H. Giessen, "Tailoring Magnetic Dipole Emission with Plasmonic Split-Ring Resonators," Phys. Rev. Lett. **111**(2), 026803 (2013).
45. J. Zhou, T. Koschny, and C. M. Soukoulis, "Magnetic and electric excitations in split ring resonators," Opt. Express **15**(26), 17881–17890 (2007).
46. M. Kauranen and A. V. Zayats, "Nonlinear plasmonics," Nat. Photonics **6**(11), 737–748 (2012).
47. M. Hentschel, M. Schäferling, X. Duan, H. Giessen, and N. Liu, "Chiral plasmonics," Sci. Adv. **3**(5), e1602735 (2017).

48. R. Blanchard, "Modeling nanoscale V-shaped antennas for the design of optical phased arrays," Phys. Rev. B **85**(15), 155457 (2012).
49. J. Sung, M. Sukharev, E. M. Hicks, R. P. Van Duyne, T. Seideman, and K. G. Spears, "Nanoparticle Spectroscopy: Birefringence in Two-Dimensional Arrays of L-Shaped Silver Nanoparticles," J. Phys. Chem. C **112**(9), 3252–3260 (2008).
50. M. Sukharev, J. Sung, K. G. Spears, and T. Seideman, "Optical properties of metal nanoparticles with no center of inversion symmetry: Observation of volume plasmons," Phys. Rev. B **76**(18), 184302 (2007).
51. R. Bukasov and J. S. Shumaker-Parry, "Highly Tunable Infrared Extinction Properties of Gold Nanocrescents," Nano Lett. **7**(5), 1113–1118 (2007).
52. R. Bukasov, T. A. Ali, P. Nordlander, and J. S. Shumaker-Parry, "Probing the Plasmonic Near-Field of Gold Nanocrescent Antennas," ACS Nano **4**(11), 6639–6650 (2010).
53. L.-J. Black, P. R. Wiecha, Y. Wang, C. H. de Groot, V. Paillard, C. Girard, O. L. Muskens, and A. Arbouet, "Tailoring Second-Harmonic Generation in Single L-Shaped Plasmonic Nanoantennas from the Capacitive to Conductive Coupling Regime," ACS Photonics **2**(11), 1592–1601 (2015).
54. J. B. Pendry, A. Aubry, D. R. Smith, and S. A. Maier, "Transformation optics and subwavelength control of light," Science **337**(6094), 549–552 (2012).
55. U. Leonhardt and T. G. Philbin, "Transformation optics and the geometry of light," in Prog. Opt. 53 (Elsevier, 2009), pp. 69–152.
56. J. B. Pendry, "Perfect cylindrical lenses," Opt. Express **11**(7), 755–760 (2003).
57. J. P. Turpin, A. T. Massoud, Z. H. Jiang, P. L. Werner, and D. H. Werner, "Conformal mappings to achieve simple material parameters for transformation optics devices," Opt. Express **18**(1), 244–252 (2010).
58. M. Kraft, Y. Luo, S. A. Maier, and J. B. Pendry, "Designing plasmonic gratings with transformation optics," Phys. Rev. X **5**(3), 031029 (2015).
59. A. K. Sheridan, A. W. Clark, A. Glidle, J. M. Cooper, and D. R. S. Cumming, "Multiple plasmon resonances from gold nanostructures," Appl. Phys. Lett. **90**(14), 143105 (2007).
60. M. Celebrano, X. Wu, M. Baselli, S. Großmann, P. Biagioni, A. Locatelli, C. De Angelis, G. Cerullo, R. Osellame, and B. Hecht, "Mode matching in multiresonant plasmonic nanoantennas for enhanced second harmonic generation," Nat. Nanotechnol. **10**(5), 412–417 (2015).
61. F. Neubrech, A. Garcia-Etxarri, D. Weber, J. Bochterle, H. Shen, M. L. De La Chapelle, G. W. Bryant, J. Aizpurua, and A. Pucci, "Defect-induced activation of symmetry forbidden infrared resonances in individual metallic nanorods," Appl. Phys. Lett. **96**(21), 213111 (2010).
62. G. Laurent, N. Félidj, J. Aubard, G. Lévi, J. R. Krenn, A. Hohenau, G. Schider, A. Leitner, and F. R. Aussenegg, "Evidence of multipolar excitations in surface enhanced Raman scattering," Phys. Rev. B **71**(4), 045430 (2005).
63. N. Kumar, A. C. Strikwerda, K. Fan, X. Zhang, R. D. Averitt, P. C. M. Planken, and A. J. L. Adam, "THz near-field Faraday imaging in hybrid metamaterials," Opt. Express **20**(10), 11277–11287 (2012).
64. A. Bitzer, H. Merbold, A. Thoman, T. Feurer, H. Helm, and M. Walther, "Terahertz near-field imaging of electric and magnetic resonances of a planar metamaterial," Opt. Express **17**(5), 3826–3834 (2009).
65. K. Zhang, "Tailoring localized surface plasmon resonances in metallic nanoantennas," Ph.D. Thesis (University of Maryland, College Park, 2020).
66. L. Novotny, "Effective wavelength scaling for optical antennas," Phys. Rev. Lett. **98**(26), 266802 (2007).
67. E. Cubukcu and F. Capasso, "Optical nanorod antennas as dispersive one-dimensional Fabry–Pérot resonators for surface plasmons," Appl. Phys. Lett. **95**(20), 201101 (2009).
68. D. Weber, P. Albella, P. Alonso-González, F. Neubrech, H. Gui, T. Nagao, R. Hillenbrand, J. Aizpurua, and A. Pucci, "Longitudinal and transverse coupling in infrared gold nanoantenna arrays: long range versus short range interaction regimes," Opt. Express **19**(16), 15047 (2011).
69. P. Berini, "Plasmon-polariton waves guided by thin lossy metal films of finite width: Bound modes of asymmetric structures," Phys. Rev. B **63**(12), 125417 (2001).
70. C. Huck, J. Vogt, T. Neuman, T. Nagao, R. Hillenbrand, J. Aizpurua, A. Pucci, and F. Neubrech, "Strong coupling between phonon-polaritons and plasmonic nanorods," Opt. Express **24**(22), 25528–25539 (2016).
71. H. Yan, T. Low, F. Guinea, F. Xia, and P. Avouris, "Tunable phonon-induced transparency in bilayer graphene nanoribbons," Nano Lett. **14**(8), 4581–4586 (2014).
72. F. Neubrech, A. Pucci, T. W. Cornelius, S. Karim, A. García-Etxarri, and J. Aizpurua, "Resonant plasmonic and vibrational coupling in a tailored nanoantenna for infrared detection," Phys. Rev. Lett. **101**(15), 157403 (2008).
73. C. Pouchert, *The Aldrich Library of FT-IR Spectra* (Wiley, 1997).
74. C. Kirk, "Quantitative analysis of the effect of disorder-induced mode coupling on infrared absorption in silica," Phys. Rev. B **38**(2), 1255–1273 (1988).
75. M. W. Klein, M. Wegener, N. Feth, and S. Linden, "Experiments on second-and third-harmonic generation from magnetic metamaterials," Opt. Express **15**(8), 5238–5247 (2007).
76. M. W. Klein, M. Wegener, N. Feth, and S. Linden, "Experiments on second-and third-harmonic generation from magnetic metamaterials: erratum," Opt. Express **16**(11), 8055 (2008).
77. H. Harutyunyan, G. Volpe, R. Quidant, and L. Novotny, "Enhancing the nonlinear optical response using multifrequency gold-nanowire antennas," Phys. Rev. Lett. **108**(21), 217403 (2012).

Optics EXPRESS

78. K. Y. Yang, J. Butet, C. Yan, G. D. Bernasconi, and O. J. F. Martin, "Enhancement Mechanisms of the Second Harmonic Generation from Double Resonant Aluminum Nanostructures," ACS Photonics **4**(6), 1522–1530 (2017).
79. D. E. Merewether, R. Fisher, and F. W. Smith, "On implementing a numeric Huygen's source scheme in a finite difference program to illuminate scattering bodies," IEEE Trans. Nucl. Sci. **27**(6), 1829–1833 (1980).
80. T. Brintlinger, A. A. Herzing, J. P. Long, I. Vurgaftman, R. Stroud, and B. S. Simpkins, "Optical dark-field and electron energy loss imaging and spectroscopy of symmetry-forbidden modes in loaded nanogap antennas," ACS Nano **9**(6), 6222–6232 (2015).
81. I. H. Malitson, "Interspecimen comparison of the refractive index of fused silica," J. Opt. Soc. Am. **55**(10), 1205–1209 (1965).